

Time-Delay Cosmography: Spectroscopy of Galaxies in the Environment of the J1537 Lensed Quasar System

G. Kharchilava,¹ E. Buckley-Geer,^{1,2} and H. Lin¹

¹*Fermi National Accelerator Laboratory*

²*Department of Astronomy & Astrophysics, University of Chicago*

(*Electronic mail: kharchilavageorge123@gmail.com)

(Dated: 11 August 2023)

Due to their sufficient distances and prevalence, lensed quasars have been a key site for research in gravitational lensing. In particular, researchers are interested in constraining Hubble’s constant by measuring time delays in the arrival times of multiply imaged quasars. However, a lens model will need to be created that accounts for not just the lensing galaxy, but also any perturbers nearby that could affect the light path. Even galaxy groups can have their influence when accounting for the group as a whole. Here, the J1537-3010 lensed quasar environment is investigated, and redshifts of 58 targets have been identified using Gemini-IRAF and The RANSAC Assisted Spectral CALibration (RASCAL) to reduce spectroscopic data from the Gemini Multi-Object Spectrograph (GMOS). An additional 19 redshifts were also supplied by the Multi Unit Spectroscopic Explorer (MUSE) from the immediate surroundings of the lensing galaxy. The success rate is roughly 45% across all four masks, less than the expected 60%-70%. We expect that masking out a bad amplifier contributed to the lower redshift calculation rate, as well as spurious wavelength solutions on the blue end. With these redshifts, flexion shifts Δ_3x were measured to determine if the observed target or identified group should be included in the lens model; only those with a $\log_{10}(\Delta_3x_{Auger}) > -4$ are considered for the lens model. An accurate lens model is fundamental for constraining the measurements of the time-delays of the quasar images and, thereby, constraining measurements for Hubble’s constant H_0 . So far, flexion shifts for all combined 77 targets were measured, as well as flexion shifts for two identified groups at $z \approx 0.394$ and $z \approx 0.587$. Only Group II and three single galaxies: objects -168, -155, & -99, all passed the flexion cut. These will need to be considered during subsequent lens modeling.

I. INTRODUCTION

Since the discovery of cosmic expansion, researchers set out to define the expansion using a parameter called Hubble’s constant H_0 . This parameter denotes the amount of space that expands at a fixed distance, per unit time. However despite numerous attempts at constraining H_0 , there has been consistent disagreement across multiple studies, especially between early and late universe measurements. Figure 1 visualizes the disagreement between the two regimes, showing disagreements of up to $4\text{-}6\sigma$, assuming a flat- Λ CDM cosmology.¹ Constraining H_0 accurately would provide great insight to cosmic expansion and efforts are underway to bridge the divorced regimes. One method researchers are utilizing is time-domain cosmology, specifically time-delay cosmography. We discuss this in Section IA and IB in more detail. Data collection and reduction is discussed in Section II and the results will be outlined in Section III. Finally, Sections IV and V will investigate the results and discuss the future direction of this work.

A. Gravitational Lensing

Einstein’s Theory of General Relativity predicts that gravity not only affects mass, but also light. With this in mind and the discovery of gravitational lensing events, researchers turned to lensed systems for cosmological measurements. Lensed supernovae were the first targets, but due to their rarity, researchers started to look at lensed quasars instead.² These ob-

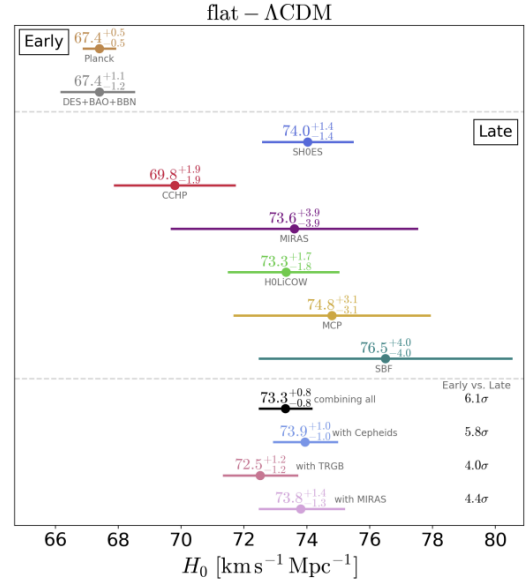


FIG. 1: H_0 measurements from across a few different studies. The two regimes, “Early” and “Late”, are shown and there is clear disagreement. Image credit: Vivien Bonvin.¹

jects are distant enough that a configuration like the one visualized in Figure 2 is more likely to occur. Another reason they make for good sites is due to their intrinsic variable luminosities (more in Section IB).

Figure 2 illustrates a typical lensing event involving a single

lensing galaxy and the source quasar. A lens model will need to be constructed that incorporates the gravitational influence of the lens. However, other galaxies in the environment of the lensing system may affect the light paths. The redshifts of these potential *perturbors* need to be measured to construct an accurate lens model. Groups are also looked at, since the combined gravitational forces of multiple galaxies may also affect the light path.

B. Time-Delays & Lens Modeling

Quasars are great sites for researching gravitational lensing not just because of their brightness and distance, but also their variable luminosity. This is important because while all lensing events have time delays, they can only be measured if the flux varies over time.

Equation 1 shows the time delay between two images A and B; where z_L is the lens redshift, D_S & D_L are the distances to the source and to the lens, respectively, D_{LS} is the distance from the lens to the source, β is vertical angle of the source above the lens plane, θ is the angle of observed position of the images, and ψ is the lensing potential for each image. Substituting the equivalences in 2, the time delay equation can be represented as Equation 3, where ϕ is known as the *Fermat potential*. We see H_0 encoded in Relation 4.

$$\Delta_{AB}(\theta) = \frac{(1+z_L) D_S D_L}{c D_{LS}} \times \left[\frac{(\vec{\theta}_A - \vec{\beta})^2}{2} - \frac{(\vec{\theta}_B - \vec{\beta})^2}{2} - \psi(\theta_A) + \psi(\theta_B) \right] \quad (1)$$

$$D_{\Delta} \equiv (1+z_L) \frac{D_S D_L}{D_{LS}} \quad \phi(\theta) \equiv \frac{(\vec{\theta} - \vec{\beta})^2}{2} - \psi(\theta) \quad (2)$$

$$\Delta_{AB}(\theta) = \frac{D_{\Delta}}{c} (\phi(\theta_A) - \phi(\theta_B)) \quad (3)$$

$$D_{\Delta} \propto H_0^{-1} \quad (4)$$

The success of constraining H_0 depends largely on the accuracy of the lens model. As aforementioned, galaxies in the environment of the lensing event need to be accounted for when constructing the model. Their influence can be quantified using the flexion shift⁵ parameter Δ_{3x} as defined in Equation 5 from a similar study⁶ done on the gravitational lenses DES J0408–5354 and WGD 2038–4008.

$$\Delta_{3x} = f(\beta) \times \left(\frac{\theta_E \theta_{E,p}}{\theta^3} \right)^2 \quad (5)$$

where

$$f(\beta) = \begin{cases} (1-\beta)^2 & \text{if } z_p > z_L \\ 1 & \text{if } z_p < z_L \end{cases} \quad (6)$$

Here, z_p is the redshift of the perturber and z_L is the redshift of the lens. θ_E and $\theta_{E,p}$ are the Einstein radii for the main lens and the perturber, respectively. β denotes a dimensionless distance product ratio involving the deflector (d), perturber (p), observer (o), and source (s) as defined as

$$\beta = \frac{D_{dp} D_{os}}{D_{op} D_{ds}} \quad (7)$$

where

$$D_{ij} = D(z_i, z_j) \quad (8)$$

is the angular diameter distance between objects i and j . A cutoff of $\log_{10}(\Delta_{3x}) > -4$ is used to determine which galaxies or groups are perturbors that need to be included in the lens modeling.

II. DATA COLLECTION AND REDUCTION

Spectroscopic images are collected at the Gemini Observatory using their Multi-Object Spectrograph (GMOS). We look at the J1537-3010 lensed quasar ‘quad’ system (see Figure 3) and its environment to identify potential perturbors. The data came with four masks (A, B, C, & D) totaling 136 targets, 12 alignment stars, and two images of the lensed quasar. We use Gemini-IRAF⁷ and RASCAL⁸ to perform reduction techniques such as wavelength calibration and flat fielding. A custom Python package is used, alongside visual inspection, to identify emission lines and determine redshifts.

A. Python Reduction

Gemini-IRAF and The RANSAC Assisted Spectral CALibration (RASCAL) package both provide a straightforward routine to perform reduction techniques on GMOS data. Following image processing and flat fielding, RASCAL is used instead of IRAF to perform wavelength calibration. Similarly to IRAF, a single slit is split up into constituents, and a wavelength solution is calculated for each slice. Then a 2D solution is fitted across the slit slices, giving us robust calibration. Though RASCAL was designed for ease of use and minimal visual inspection, the process of including arc features that RASCAL could identify was non trivial for the blue B600 setting on GMOS. The presence of more lines tended to cause RASCAL to misidentify features that were close in proximity to one another. A new, updated version of the wavelength calibration script has been created by Huan Lin to address this issue. Instead of the previous method, it uses tracing to keep the correctly identified lines static across multiple slices.

1. Additional Routines

After wavelength solutions are applied and multiple spectroscopic settings are combined, a custom Python package

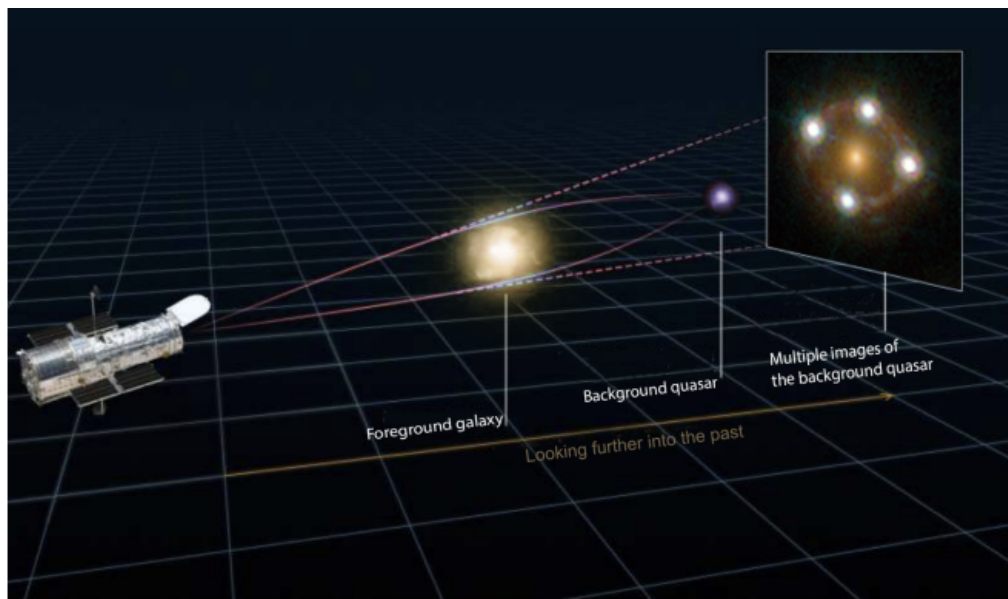


FIG. 2: Diagram of a typical lensing event. Light from the background quasar is lensed by a massive object, usually a galaxy but sometimes a group of galaxies. Note that lensing events may not be this ideal or symmetric, sometimes appearing three or less times and asymmetrically. Quasar image credit: Kenneth C. Wong³. Diagram credit: Martin Millon⁴

`setz_gemini` takes each reduced slit and displays them. The slits are then visually observed and if emission lines are found, the package will label them based on the input templates. Figure 6 shows a 2D spectroscopic image of object 216, along with the emission line identifications outputted from the routine. This routine also lets the user assign confidence levels based on number of emission lines detected. Confidence of 4

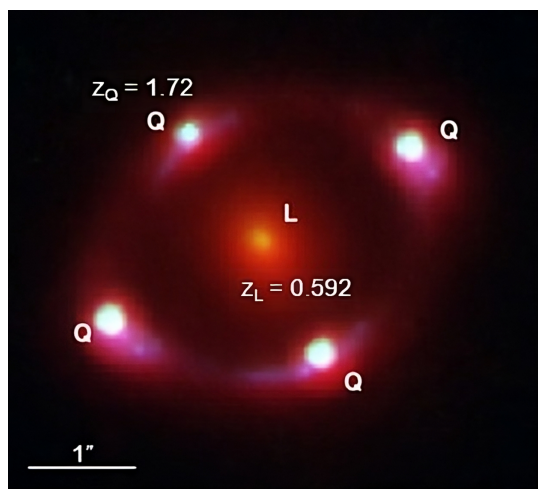


FIG. 3: Lensed quasar from data set J1537-3010 in an RGB color composite image made using HST Wide Field Camera 3 (WFC3) data. ‘L’ denotes the position of the lensing galaxy and ‘Q’ denotes the lensed quasar. Each instance of ‘Q’ is the same quasar being imaged four times. We are interested in the time-delay of the arrival times of each of these images. Image credit: Elizabeth Buckley-Geer.

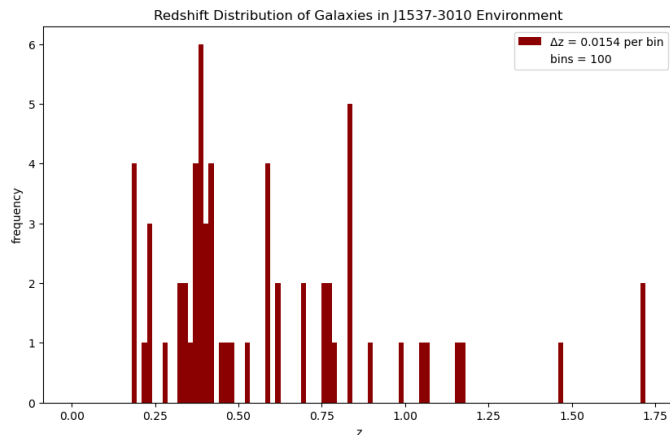


FIG. 4: The histogram shows the redshift frequency for the objects which have confident redshift measurements. The confidence is based on abundance of emission lines and data quality. Only those with confidences of 3 or 4 were considered here.

is multi-line certain, while 3 denotes single-line confidence, 2 is uncertain, and 9 for no emission lines found. We methodically calculate the flexion shifts for individual galaxies using redshift data derived from the `setz_gemini` custom package. Single galaxy flexion shift calculations require velocity dispersions and our methodology outlines two distinct methods to ascertain these velocity dispersions, each resulting in a specific flexion shift value. A more thorough discussion of these approaches is discussed in Section IV. A group finding routine `simple_group_finder` written by Jason Poh⁹ is also employed to detect groups and measure group flex-

ion shifts. The individual galaxy flexion shifts, along with the i-band magnitudes, redshifts, etc. are shown in Table I.

III. RESULTS

A total of 62 redshifts were confidently (3 or 4) measured from all of the four masks. Of those, two redshift measurements were for the quasar, one had bad photometry, and another one had missing parameters. This means that from the 136 targets taken by GMOS, 58 confident redshifts were measured. The masks A,B,C, and D had successful redshift calculation rates of 44%, 54%, 39%, and 45%, respectively. There were more redshift measurements with lower confidences (2), but those targets had single emission lines visible so some inference was needed. The rest of the targets had no visible emission lines and therefore, had no spectroscopic redshift measurements. In addition to the GMOS data, an additional 19 redshifts were supplied by the Multi Unit Spectroscopic Explorer (MUSE), which is a panoramic integral-field spectrograph.¹⁰ Since we believe these targets are more influential to the lensing environment, we utilized MUSE to focus on the surroundings of the lensing galaxy for our observations. A histogram of both GMOS and MUSE data is plotted in Figure 4 to determine potential galactic structures and to see the redshift ranges. The two objects to the far right is the quasar, with $z = 1.72$. Table I displays all the object information for the GMOS+MUSE data that had redshift and flexion measurements.

IV. DISCUSSION

As previously mentioned, we only include targets in the lens model that make the flexion cut as defined in Section I B. For single galaxies, two flexion shifts are calculated using two different velocity dispersions σ for the perturber Einstein radius $\theta_{E,p}$ as defined as

$$\theta_{E,p} = 4\pi \left(\frac{\sigma}{c} \right)^2 \frac{D_{ps}}{D_{os}} \quad (9)$$

assuming a Singular Isothermal Sphere (SIS)⁶ model. These two velocity dispersions come from two different scaling methods from Zahid¹¹ and Auger¹², where the latter is constructed with higher mass elliptical galaxies.

We use Auger calculations for our cut due to its more conservative estimates. Of the 77 total targets from both GMOS and MUSE, three targets made the flexion cut resolved within error bars when measuring single galaxy flexion shifts. These were objects -168, -155, and -99, all of which are listed in Table I with a $\log_{10}(\Delta_{3x_{Auger}}) = -3.27^{+0.21}_{-0.23}$, $-3.60^{+0.24}_{-0.26}$, & $-4.03^{+0.21}_{-0.22}$, respectively.

Next, group flexion shifts are measured; the largest peak at $z \approx 0.394$ in Figure 4 indicates the presence of a galaxy group, which was further confirmed by `simple_group_finder` and labeled as Group I. The increased counts at $z \approx 0.587$ was

also identified and labeled as Group II. Despite the considerable galaxy density in Group I, its flexion shift, denoted by $\log_{10}(\Delta_{3x})_I = -4.22$, does not meet the necessary threshold. In contrast, Group II, with a less dense galaxy distribution, achieves the threshold with a flexion shift of $\log_{10}(\Delta_{3x})_{II} = -3.64$. This is attributed to Group II's closer proximity to the lensing galaxy, which places it more directly along the line of sight to the source. As a result, Group II will be included in subsequent lens modeling.

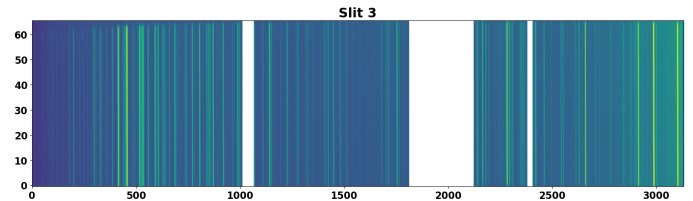


FIG. 5: 2D image of slit 3 from an arc image. You can see the masked out chip gaps, but also a giant masked out region due to a malfunction in an amplifier.

The efficacy of the masks was evaluated in comparison to prior observations, and it was found that the masks associated with these specific GMOS observations demonstrated lower than expected success rates of $\sim 45\%$. Typically, we anticipate masks to exhibit success rates in the range of 60%-70%. However, for the four masks pertaining to J1537, we observed a reduction of approximately 25%. One plausible explanation for this could be that emission lines were situated within a defective amplifier region, leading to a portion of the CCD being masked out due to amplifier 5 malfunction. This can be distinctly observed in Figure 5, where the masked region is clearly visible. Issues were also encountered with the wavelength calibration of the blue setting of the masks. The abundance of arc lines led RASCAL to generate erroneous solutions, which could potentially lower confidence levels if emission lines are obscured by inaccurate wavelength calibrations. Additionally, issues with the combination routine arose that caused the interpolated and defected regions to still appear. Viewing conditions may have also played a role, but it is unlikely since this particular data was from priority 1 observations.

V. CONCLUSIONS

The data collected in this study forms part of a broader collaborative effort aimed at measuring a range of different lensed systems to constrain H_0 . In addition to the currently available reduction-ready data, proposals for further observations using GMOS have been approved. The application of Huan's updated wavelength calibration routine will not only streamline the process but also future observations will be conducted with a fixed amplifier. These enhancements to our GMOS reduction pipeline are expected to yield higher success rates.

The identification of objects -168, -155, -99, and Group II,

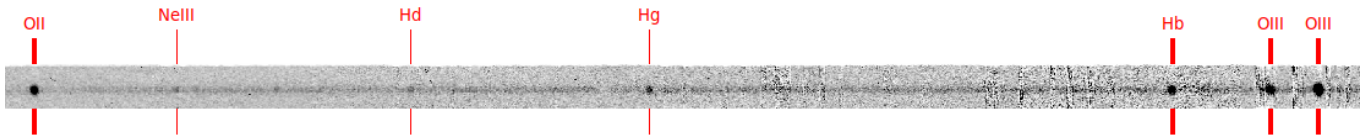


FIG. 6: Above is a 2D spectrum of object 216 from Mask B. The galaxy’s redshift is $z = 0.77166$. The prevalence of so many lines gives this redshift calculation a confidence of 4.

all exhibiting flexion shifts that meet the threshold within error bars, will be crucial for the lens modeling of the J1537 system. As previously noted, an accurate model is important for time-delay calculations, all of which contribute to constraining H_0 . Alongside previous and upcoming observations, this analysis will be used to further our understanding of cosmic expansion.

ACKNOWLEDGMENTS

This work was supported in part by the U.S. Department of Energy, Office of Science, Office of Workforce Development for Teachers and Scientists (WDTS) under the Science Undergraduate Laboratory Internships Program (SULI). I would like to thank both my supervisor Professor Elizabeth Buckley-Geer and co-supervisor Professor Huan Lin for their guidance and mentorship throughout the duration of my SULI.

¹L. Verde, T. L. Treu, and A. G. Riess, “Tensions between the early and late universe,” *Nature Astronomy* **3**, 891 – 895 (2019).

²R. Narayan and M. Bartelmann, “Lectures on gravitational lensing,” (1997), arXiv:astro-ph/9606001 [astro-ph].

³K. C. Wong, S. H. Suyu, M. W. Auger, V. Bonvin, F. Courbin, C. D. Fassnacht, A. Halkola, C. E. Rusu, D. Sluse, A. Sonnenfeld, T. Treu, T. E. Collett, S. Hilbert, L. V. E. Koopmans, P. J. Marshall, and N. Rumbaugh, “H0LiCOW – IV. Lens mass model of HE 04351223 and blind measurement of its time-delay distance for cosmology,” *Monthly Notices of the Royal Astronomical Society* **465**, 4895–4913 (2016), <https://academic.oup.com/mnras/article-pdf/465/4/4895/10255170/stw3077.pdf>.

⁴S. Birrer, M. Millon, D. Sluse, A. J. Shajib, F. Courbin, L. V. E. Koopmans, S. H. Suyu, and T. Treu, “Time-delay cosmography: Measuring the hubble constant and other cosmological parameters with strong gravitational lensing,” (2023), arXiv:2210.10833 [astro-ph.CO].

⁵C. McCully, C. R. Keeton, K. C. Wong, and A. I. Zabludoff, “Quantifying environmental and line-of-sight effects in models of strong gravitational lens systems,” *The Astrophysical Journal* **836**, 141 (2017).

⁶E. J. Buckley-Geer, H. Lin, C. E. Rusu, J. Poh, A. Palmese, A. Agnello, L. Christensen, J. Frieman, A. J. Shajib, T. Treu, T. Collett, S. Birrer, T. Anguita, C. D. Fassnacht, G. Meylan, S. Mukherjee, K. C. Wong, M. Aguena, S. Allam, S. Avila, E. Bertin, S. Bhargava, D. Brooks, A. Carnero Rosell, M. Carrasco Kind, J. Carretero, F. J. Castander, M. Costanzi, L. N. da Costa, J. De Vicente, S. Desai, H. T. Diehl, P. Doel, T. F. Eifler, S. Everett, B. Flaugher, P. Fosalba, J. Garcia-Bellido, E. Gaztanaga, D. Gruen, R. A. Gruendl, J. Gschwend, G. Gutierrez, S. R. Hinton, K. Honscheid, D. J. James, K. Kuehn, N. Kuropatkin, M. A. G. Maia, J. L. Marshall, P. Melchior, F. Menanteau, R. Miquel, R. L. C. Ogando, F. Paz-Chinchón, A. A. Plazas, E. Sanchez, V. Scarpine, M. Schubnell, S. Serrano, I. Sevilla-Noarbe, M. Smith, M. Soares-Santos, E. Suchyta, M. E. C. Swanson, G. Tarle, D. L. Tucker, T. N. Varga, and T. D. Collaboration, “STRIDES: Spectroscopic and photometric characterization of the environment and effects of mass along the line of sight to the gravitational lenses DES J0408–5354 and WGD 2038–4008,” *Monthly Notices of the Royal Astronomical Society* **498**, 3241–3274 (2020), <https://academic.oup.com/mnras/article-pdf/498/3/3241/33780687/staa2563.pdf>.

⁷Gemini Observatory and AURA, “Gemini IRAF: Data reduction software for the Gemini telescopes,” *Astrophysics Source Code Library*, record ascl:1608.006 (2016), ascl:1608.006.

⁸J. Veitch–Michaelis and M. C. Lam, “RASCAL: Towards Automated Spectral Wavelength Calibration,” in *Astronomical Data Analysis Software and Systems XXIX*, *Astronomical Society of the Pacific Conference Series*, Vol. 527, edited by R. Pizzo, E. R. Deul, J. D. Mol, J. de Plaa, and H. Verkerker (2020) p. 627, arXiv:1912.05883 [astro-ph.IM].

⁹Graduate Student at the Department of Astronomy & Astrophysics, University of Chicago.

¹⁰R. Bacon, M. Accardo, L. Adjali, H. Anwand, S. Bauer, I. Biswas, J. Blaizot, D. Boudon, S. Brau-Nogue, J. Brinchmann, P. Caillier, L. Capoen, C. M. Carollo, T. Contini, P. Couderc, E. Daguise, S. Deiries, B. Delabre, S. Dreizler, J. Dubois, M. Dupieux, C. Dupuy, E. Emsellem, T. Fechner, A. Fleischmann, M. François, G. Gallou, T. Gharsa, A. Glin-demann, D. Gojak, B. Guiderdoni, G. Hansali, T. Hahn, A. Jarno, A. Kelz, C. Koehler, J. Kosmowski, F. Laurent, M. Le Floch, S. J. Lilly, J. L. Lizon, M. Loupiau, A. Manescau, C. Monstein, H. Nicklas, J. C. Olaya, L. Pares, L. Pasquini, A. Pécontal-Rousset, R. Pelló, C. Petit, E. Popow, R. Reiss, A. Remillieux, E. Renault, M. Roth, G. Rupprecht, D. Serre, J. Schaye, G. Soucaill, M. Steinmetz, O. Streicher, R. Stuijk, H. Valentin, J. Vernet, P. Weilbacher, L. Wisotzki, and N. Yerle, “The MUSE second-generation VLT instrument,” in *Ground-based and Airborne Instrumentation for Astronomy III*, *Society of Photo-Optical Instrumentation Engineers (SPIE) Conference Series*, Vol. 7735, edited by I. S. McLean, S. K. Ramsay, and H. Takami (2010) p. 773508, arXiv:2211.16795 [astro-ph.IM].

¹¹H. J. Zahid, M. J. Geller, D. G. Fabricant, and H. S. Hwang, “The scaling of stellar mass and central stellar velocity dispersion for quiescent galaxies at $z < 0.7$,” *The Astrophysical Journal* **832**, 203 (2016).

¹²M. W. Auger, T. Treu, B. J. Brewer, and P. J. Marshall, “A compact early-type galaxy at $z = 0.6$ under a magnifying lens: evidence for inside-out growth,” *Monthly Notices of the Royal Astronomical Society: Letters* **411**, L6–L10 (2011), <https://academic.oup.com/mnrasl/article-pdf/411/1/L6/6202661/411-1-L6.pdf>.

Appendix A: Group Finder & Galaxy Catalogue

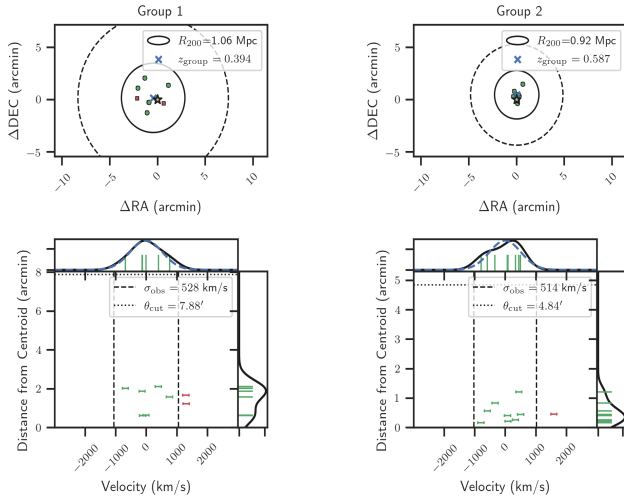


FIG. 7: Identification of Groups I and II using spectroscopic samples from J1537. The first row of plots with the coordinates RA and Dec show group member candidates. The star denotes the lensing galaxy, while the green points denote group candidates that became members and red denotes candidates that were not included as members. The group centroid is shown with the blue cross and the dotted circle is the angular separation cut of the group-finding algorithm in its final iteration. The plots on the bottom row shows the observer-frame velocity of individual member galaxies relative to the group centroid as a function of that galaxy’s angular distance from the centroid. The final observer-frame velocity dispersion and angular separation cuts from the group-finding algorithm are presented as dashed and dotted lines, respectively and the red and green points indicate the very same members that were added. A histogram, along with a Gaussian fit is also shown.⁶

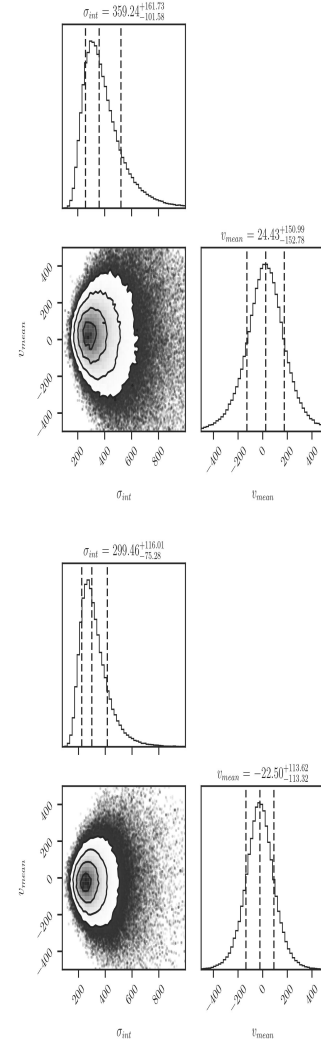


FIG. 8: Corner plots from `simple_group_finder`

Object ID	RA (deg)	Dec (deg)	z	i-band (mag)	$\log_{10}(M_*)$ ($\log_{10}(M_{\odot})$)	$\Delta \theta$ (arcsec)	$\log_{10}(\Delta z_{\text{Zahid}})$ ($\log_{10}(\text{arcsec})$)	$\log_{10}(\Delta z_{\text{Auger}})$ ($\log_{10}(\text{arcsec})$)	Object ID	RA (deg)	Dec (deg)	z	i-band (mag)	$\log_{10}(M_*)$ ($\log_{10}(M_{\odot})$)	$\Delta \theta$ (arcsec)	$\log_{10}(\Delta z_{\text{Zahid}})$ ($\log_{10}(\text{arcsec})$)	$\log_{10}(\Delta z_{\text{Auger}})$ ($\log_{10}(\text{arcsec})$)
-168	234.357609	-30.173165	0.58473	21.798	$10.38^{+0.09}_{-0.14}$	9.1	$-3.75^{+0.40}_{-0.55}$	$-3.27^{+0.21}_{-0.23}$	-9029	234.344852	-30.172455	0.98095	23.835	$9.42^{+0.31}_{-0.29}$	33.7	$-8.25^{+0.72}_{-1.06}$	$-6.97^{+0.30}_{-0.30}$
-155	234.353989	-30.172060	0.73008	22.845	$9.70^{+0.20}_{-0.22}$	5.6	$-4.64^{+0.59}_{-0.89}$	$-3.60^{+0.24}_{-0.26}$	1543	234.390633	-30.153513	0.38282	21.227	$9.74^{+0.11}_{-0.13}$	126.5	$-7.97^{+0.54}_{-0.80}$	$-6.97^{+0.21}_{-0.23}$
-99	234.358184	-30.166900	0.58698	21.576	$10.55^{+0.08}_{-0.10}$	17.9	$-4.44^{+0.38}_{-0.49}$	$-4.03^{+0.22}_{-0.22}$	1314	234.387028	-30.180743	0.35061	22.749	$9.28^{+0.16}_{-0.21}$	103.5	$-8.41^{+0.62}_{-0.99}$	$-7.00^{+0.23}_{-0.26}$
-80	234.360919	-30.165461	0.58781	19.868	$10.88^{+0.06}_{-0.10}$	26.9	$-4.58^{+0.33}_{-0.42}$	$-4.33^{+0.20}_{-0.21}$	1837	234.383198	-30.205516	0.19349	18.836	$9.75^{+0.08}_{-0.07}$	150.0	$-8.00^{+0.53}_{-0.76}$	$-7.01^{+0.21}_{-0.21}$
-59	234.359337	-30.163633	0.58404	20.199	$10.99^{+0.05}_{-0.05}$	30.1	$-4.59^{+0.31}_{-0.37}$	$-4.39^{+0.20}_{-0.20}$	1492	234.378974	-30.176438	0.75158	22.419	$9.66^{+0.18}_{-0.23}$	75.0	$-8.15^{+0.59}_{-0.92}$	$-7.07^{+0.23}_{-0.27}$
-214	234.357905	-30.177723	0.58556	21.257	$10.53^{+0.07}_{-0.18}$	24.1	$-4.85^{+0.38}_{-0.49}$	$-4.43^{+0.21}_{-0.21}$	920	234.368641	-30.146779	0.58816	21.440	$9.39^{+0.13}_{-0.12}$	97.3	$-8.39^{+0.60}_{-0.91}$	$-7.08^{+0.22}_{-0.21}$
-90	234.349275	-30.166768	0.58693	21.172	$10.56^{+0.08}_{-0.18}$	25.7	$-4.90^{+0.38}_{-0.53}$	$-4.50^{+0.21}_{-0.24}$	-25	234.359110	-30.159988	0.73239	24.147	$8.39^{+0.29}_{-0.26}$	42.3	$-9.37^{+0.47}_{-0.42}$	$-7.17^{+0.28}_{-0.28}$
-5	234.350957	-30.158310	0.58836	19.739	$11.09^{+0.07}_{-0.18}$	49.1	$-5.12^{+0.29}_{-0.41}$	$-4.96^{+0.20}_{-0.24}$	930	234.342774	-30.185505	0.83299	21.873	$9.55^{+0.19}_{-0.16}$	64.8	$-8.39^{+0.61}_{-0.83}$	$-7.22^{+0.24}_{-0.24}$
-232	234.352112	-30.179351	0.56920	21.419	$10.19^{+0.10}_{-0.11}$	30.8	$-5.59^{+0.45}_{-0.60}$	$-4.98^{+0.21}_{-0.22}$	165	234.315995	-30.153192	0.39333	21.707	$9.53^{+0.11}_{-0.13}$	139.5	$-8.43^{+0.58}_{-0.87}$	$-7.25^{+0.21}_{-0.22}$
-11	234.348588	-30.159554	0.60138	20.813	$10.57^{+0.14}_{-0.12}$	47.7	$-5.73^{+0.40}_{-0.50}$	$-5.33^{+0.22}_{-0.22}$	1818	234.374693	-30.147514	0.37589	21.915	$8.92^{+0.20}_{-0.16}$	104.3	$-9.02^{+0.58}_{-0.80}$	$-7.29^{+0.24}_{-0.23}$
1648	234.373728	-30.165172	0.46538	20.278	$10.53^{+0.10}_{-0.14}$	60.6	$-5.93^{+0.39}_{-0.51}$	$-5.51^{+0.21}_{-0.23}$	139	234.323686	-30.139219	0.41729	21.564	$9.50^{+0.13}_{-0.17}$	152.4	$-8.62^{+0.59}_{-0.91}$	$-7.41^{+0.22}_{-0.24}$
703	234.339385	-30.170891	0.33634	21.195	$9.99^{+0.08}_{-0.09}$	50.5	$-6.32^{+0.48}_{-0.67}$	$-5.54^{+0.21}_{-0.21}$	1731	234.351032	-30.193692	0.83274	22.343	$9.69^{+0.20}_{-0.18}$	87.7	$-8.47^{+0.60}_{-0.85}$	$-7.43^{+0.24}_{-0.24}$
-117	234.348089	-30.168578	0.74487	22.619	$9.58^{+0.22}_{-0.25}$	25.4	$-6.83^{+0.63}_{-0.83}$	$-5.69^{+0.25}_{-0.27}$	420	234.342839	-30.137777	0.59348	22.050	$9.38^{+0.22}_{-0.14}$	127.2	$-8.76^{+0.65}_{-0.95}$	$-7.44^{+0.25}_{-0.23}$
872	234.342955	-30.183665	0.23615	19.179	$9.92^{+0.18}_{-0.24}$	59.3	$-6.56^{+0.54}_{-0.83}$	$-5.72^{+0.23}_{-0.27}$	147	234.323278	-30.139215	0.41817	22.186	$9.46^{+0.15}_{-0.16}$	153.3	$-8.69^{+0.60}_{-0.92}$	$-7.45^{+0.22}_{-0.24}$
757	234.358562	-30.148531	0.38210	19.491	$10.52^{+0.07}_{-0.18}$	82.6	$-6.26^{+0.38}_{-0.49}$	$-5.84^{+0.20}_{-0.24}$	1699	234.352178	-30.196562	0.41899	22.790	$8.53^{+0.18}_{-0.17}$	91.4	$-9.53^{+0.31}_{-0.44}$	$-7.45^{+0.24}_{-0.24}$
-203	234.347935	-30.176373	0.61811	22.596	$9.07^{+0.18}_{-0.17}$	30.0	$-7.45^{+0.61}_{-0.91}$	$-5.86^{+0.23}_{-0.24}$	520	234.323021	-30.177308	0.17897	21.744	$8.36^{+0.08}_{-0.08}$	103.6	$-9.74^{+0.13}_{-0.13}$	$-7.51^{+0.21}_{-0.21}$
-245	234.358061	-30.180583	0.46560	23.151	$8.87^{+0.23}_{-0.25}$	34.1	$-7.74^{+0.58}_{-0.84}$	$-5.96^{+0.25}_{-0.27}$	1860	234.338742	-30.198130	0.75648	22.669	$9.63^{+0.21}_{-0.19}$	109.8	$-8.70^{+0.62}_{-0.83}$	$-7.60^{+0.25}_{-0.28}$
877	234.335014	-30.192786	0.39632	20.700	$10.66^{+0.04}_{-0.05}$	100.3	$-6.36^{+0.36}_{-0.45}$	$-6.01^{+0.20}_{-0.20}$	1941	234.381616	-30.212380	0.23476	20.914	$9.10^{+0.09}_{-0.10}$	168.5	$-9.23^{+0.58}_{-0.87}$	$-7.66^{+0.21}_{-0.21}$
-182	234.353658	-30.174605	1.00015	23.669	$8.91^{+0.24}_{-0.31}$	13.2	$-7.92^{+0.71}_{-0.95}$	$-6.18^{+0.31}_{-0.31}$	1197	234.359485	-30.203482	0.98832	20.516	$10.72^{+0.04}_{-0.04}$	116.3	$-8.00^{+0.35}_{-0.44}$	$-7.67^{+0.20}_{-0.20}$
1592	234.373783	-30.159057	0.48223	22.070	$9.80^{+0.14}_{-0.17}$	71.8	$-7.22^{+0.54}_{-0.80}$	$-6.28^{+0.22}_{-0.24}$	782	234.335507	-30.183533	1.05973	22.249	$10.30^{+0.16}_{-0.18}$	76.4	$-8.20^{+0.43}_{-0.58}$	$-7.69^{+0.23}_{-0.24}$
1793	234.377686	-30.148294	0.39150	20.761	$10.41^{+0.07}_{-0.08}$	107.7	$-6.74^{+0.41}_{-0.51}$	$-6.28^{+0.21}_{-0.21}$	220	234.330007	-30.137203	0.39511	22.082	$9.00^{+0.19}_{-0.13}$	146.5	$-9.36^{+0.60}_{-0.84}$	$-7.70^{+0.24}_{-0.22}$
1603	234.381499	-30.161665	0.62488	21.299	$10.42^{+0.12}_{-0.17}$	87.8	$-6.77^{+0.41}_{-0.55}$	$-6.31^{+0.22}_{-0.24}$	511	234.323658	-30.174925	0.83558	21.913	$9.53^{+0.14}_{-0.16}$	100.2	$-9.00^{+0.59}_{-0.90}$	$-7.82^{+0.22}_{-0.24}$
-66	234.342807	-30.164174	0.38160	21.356	$8.82^{+0.08}_{-0.09}$	47.4	$-8.17^{+0.47}_{-0.65}$	$-6.35^{+0.21}_{-0.21}$	325	234.339344	-30.133336	0.45486	22.807	$9.90^{+0.27}_{-0.31}$	145.8	$-9.57^{+0.64}_{-0.94}$	$-7.82^{+0.27}_{-0.31}$
1714	234.373956	-30.161102	0.21994	20.716	$9.22^{+0.11}_{-0.12}$	68.0	$-7.84^{+0.59}_{-0.91}$	$-6.38^{+0.21}_{-0.22}$	216	234.325391	-30.143733	0.77163	21.290	$9.60^{+0.13}_{-0.10}$	136.8	$-9.09^{+0.58}_{-0.83}$	$-7.96^{+0.22}_{-0.21}$
1599	234.382550	-30.159762	0.52126	21.882	$10.13^{+0.12}_{-0.13}$	93.7	$-7.08^{+0.47}_{-0.64}$	$-6.43^{+0.21}_{-0.22}$	1303	234.409422	-30.142616	0.59349	21.533	$9.44^{+0.13}_{-0.13}$	196.9	$-9.24^{+0.59}_{-0.90}$	$-7.97^{+0.22}_{-0.22}$
1550	234.366792	-30.187827	0.70177	21.645	$10.16^{+0.12}_{-0.14}$	68.8	$-7.05^{+0.46}_{-0.63}$	$-6.43^{+0.22}_{-0.25}$	206	234.307989	-30.168822	0.76968	21.778	$9.72^{+0.21}_{-0.20}$	148.5	$-8.99^{+0.60}_{-0.86}$	$-7.97^{+0.25}_{-0.25}$
-1	234.364935	-30.183139	0.17508	22.308	$8.59^{+0.17}_{-0.19}$	51.5	$-8.46^{+0.34}_{-0.40}$	$-6.43^{+0.23}_{-0.25}$	716	234.369168	-30.125799	0.69254	22.999	$9.50^{+0.21}_{-0.24}$	169.3	$-9.26^{+0.63}_{-0.98}$	$-8.05^{+0.24}_{-0.27}$
694	234.356388	-30.144301	0.19225	20.226	$9.60^{+0.07}_{-0.07}$	97.4	$-7.68^{+0.56}_{-0.82}$	$-6.55^{+0.21}_{-0.21}$	1345	234.403145	-30.152441	0.41516	22.970	$8.67^{+0.26}_{-0.33}$	162.9	$-10.05^{+0.51}_{-0.70}$	$-8.09^{+0.27}_{-0.32}$
281	234.315092	-30.169888	0.39812	20.272	$10.25^{+0.06}_{-0.07}$	126.2	$-7.15^{+0.42}_{-0.56}$	$-6.60^{+0.20}_{-0.21}$	187	234.316482	-30.153627	0.78743	22.504	$9.44^{+0.19}_{-0.20}$	137.4	$-9.40^{+0.63}_{-0.96}$	$-8.14^{+0.24}_{-0.25}$
807	234.362551	-30.146281	0.37808	20.273	$9.61^{+0.10}_{-0.13}$	92.8	$-7.76^{+0.56}_{-0.82}$	$-6.65^{+0.21}_{-0.21}$	436	234.315943	-30.179164	0.28492	22.793	$7.96^{+0.18}_{-0.15}$	126.6	$-10.75^{+0.28}_{-0.24}$	$-8.16^{+0.23}_{-0.23}$
771	234.338648	-30.176013	0.39338	22.501	$8.55^{+0.13}_{-0.14}$	55.4	$-8.81^{+0.25}_{-0.28}$	$-6.75^{+0.22}_{-0.23}$	1926	234.416501	-30.162563	0.82910	22.011	$10.08^{+0.17}_{-0.19}$	192.2	$-8.94^{+0.51}_{-0.71}$	$-8.25^{+0.23}_{-0.25}$
768	234.338172	-30.175913	0.39376	22.777	$8.59^{+0.14}_{-0.14}$	56.7	$-8.78^{+0.30}_{-0.33}$	$-6.75^{+0.22}_{-0.23}$	1332	234.407656	-30.144473	0.61639	22.811	$9.07^{+0.24}_{-0.21}$	188.7	$-9.85^{+0.65}_{-0.94}$	$-8.25^{+0.26}_{-0.25}$
381	234.330793	-30.152613	0.32677	21.596	$9.54^{+0.10}_{-0.11}$	102.5	$-7.96^{+0.57}_{-0.86}$	$-6.78^{+0.21}_{-0.22}$	199	234.331336	-30.132870	0.17994	22.494	$8.04^{+0.13}_{-0.13}$	157.8	$-10.81^{+0.21}_{-0.21}$	$-8.29^{+0.22}_{-0.22}$
1457	234.374002	-30.186786	0.22797	21.968	$8.91^{+0.11}_{-0.13}$	79.8	$-8.56^{+0.53}_{-0.77}$	$-6.82^{+0.21}_{-0.22}$	557	234.361929	-30.121841	0.83347	22.678	$9.68^{+0.20}_{-0.25}$	179.3	$-9.51^{+0.60}_{-0.93}$	$-8.46^{+0.24}_{-0.27}$
-223	234.368369	-30.177746	0.39814	23.991	$8.12^{+0.31}_{-0.34}$	45.9	$-9.27^{+0.50}_{-0.59}$	$-6.82^{+0.20}_{-0.27}$	1263	234.386802	-30.184845	1.16572	22.536	$10.02^{+0.13}_{-0.15}$	108.6	$-9.52^{+0.49}_{-0.70}$	$-8.76^{+0.22}_{-0.23}$
616	234.345908	-30.152754	0.59395	21.467	$9.20^{+0.15}_{-0.13}$	73.4	$-8.34^{+0.61}_{-0.92}$	$-6.86^{+0.23}_{-0.22}$	324	234.334695	-30.140246	1.05276	22.839	$9.68^{+0.26}_{-0.26}$	129.5	$-9.85^{+0.65}_{-0.96}$	$-8.80^{+0.27}_{-0.29}$
1556	234.377676	-30.171076	0.32451	22.191	$8.66^{+0.17}_{-0.16}$	68.7	$-8.85^{+0.40}_{-0.47}$	$-6.89^{+0.23}_{-0.23}$	1205	234.398681	-30.153766	0.89875	22.936	$8.97^{+0.26}_{-0.21}$	148.3	$-10.63^{+0.65}_{-0.89}$	$-8.94^{+0.27}_{-0.26}$
1583	234.373993	-30.171483	0.37672	22.814	$8.39^{+0.12}_{-0.13}$	57.2	$-9.11^{+0.19}_{-0.21}$	$-6.90^{+0.22}_{-0.22}$	1074	234.417546	-30.157010	1.15314	22.574	$9.99^{+0.22}_{-0.22}$	199.6	$-10.30^{+0.56}_{-0.76}$	$-9.53^{+0.25}_{-0.25}$
									1538	234.391266	-30.154170	1.46086	22.751	$8.96^{+0.23}_{-0.24}$	127.1	$-13.02^{+0.62}_{-0.91}$	$-11.33^{+0.25}_{-0.27}$

TABLE I: All catalogued targets from the J1537 environment using GMOS+MUSE with confident redshift measurements and log of flexion shifts. Negative object ID numbers denote MUSE targets and positive denotes GMOS targets.